X-621-71-422
PREPRINT

A THEORETICAL MODEL OF THE IONOSPHERE DYNAMICS WITH INTERHEMISPHERIC COUPLING

H. G. MAYR
E. G. FONTHEIM
L. H. BRACE
H. C. BRINTON
H. A. TAYLOR, JR.

OCTOBER 1971

GSFC
GODDARD SPACE FLIGHT CENTER
GREENBELT, MARYLAND

PAPER PRESENTED AT THE CONFERENCE ON THEORETICAL IONOSPHERE MODELS, AT UNIVERSITY PARK, PA., JUNE 14 – 16, 1971

A THEORETICAL MODEL OF THE IONOSPHERE DYNAMICS WITH INTERHEMISPHERIC COUPLING

by

H. G. Mayr*

E. G. Fontheim**

L. H. Brace*

H. C. Brinton*

and

H. A. Taylor, Jr.*

*Thermosphere and Exosphere Branch
Goddard Space Flight Center
Greenbelt, Maryland

**Space Physics Research Laboratory
University of Michigan
Ann Arbor, Michigan

A THEORETICAL MODEL OF THE IONOSPHERE DYNAMICS WITH INTERHEMISPHERIC COUPLING

by

H. G. Mayr*

E. G. Fontheim**

L. H. Brace*

H. C. Brinton*

and

H. A. Taylor, Jr.*

*Thermosphere and Exosphere Branch
Goddard Space Flight Center
Greenbelt, Maryland

**Space Physics Research Laboratory
University of Michigan
Ann Arbor, Michigan

Abstract

The ionospheric plasma is described by means of the momentum and continuity equations for O^+, He^+, H^+ and the energy equations for T_e and T_i. The ion production rate profiles and the photoelectron heating rates to the plasma are computed separately and serve as source functions in the continuity and energy equations respectively. The neutral atmosphere (composition, winds, temperature) as well as the incident photon spectrum are part of the inputs. Charge transfer, collisional energy loss processes, ion-neutral drag, diffusion and electron heat conduction are among the physical processes included in the calculations. Ion heat conduction is neglected. Assuming steady state, the equations are transformed into integral equations and then solved iteratively along geomagnetic field lines from the region of chemical equilibrium up to the equatorial plane. In this scheme non local heating is included in a self-consistent way. The lower boundary conditions are obtained by satisfying photochemical and local energy equilibrium. Under conditions of asymmetry with respect to the equatorial plane the solutions are carried out for both hemispheres and the upper boundary conditions are determined by requiring continuity of the physical parameters across the equatorial plane. In this way interhemispheric plasma transport is introduced in a natural way. For symmetric conditions the transport fluxes are assumed zero at the equator. An extension of this model to include time dependent phenomena is presented.

CONTENTS

FIGURE CAPTIONS

FIGURE CAPIONS

I. Introduction

The model presented here has provided the theoretical framework for the interpretation of satellite and rocket data on the ion composition and plasma temperatures (Mayr et al., 1967, Mayr et al., 1968, Brace et al., 1969, Brinton et al., 1969, Mayr and Brace, 1970, Mayr et al., 1970a, Brinton et al., 1971, Mayr, 1968, Brinton et al., 1970, Brace et al., 1970, Mayr et al., 1970b).

In general, density and temperature gradients along field lines cannot be obtained from satellite data nor do those data provide information on the transport fluxes directly. For this reason it is desirable to eliminate uncertainties associated with the choice of upper boundary conditions (which require the knowledge of transport fluxes) as far as possible. In the interest of this objective we have therefore chosen to integrate the continuity, momentum, and energy equations along field lines up to the equatorial plane, thereby eliminating the boundary value problem.

The calculations presented in this paper cover the F_2 region and the protonosphere since satellite orbits rarely dip below the F_2 region. This simplifies the analysis in a number of respects considerably since in that case the model can be restricted to a three constituent plasma with the ion species, O^+, H_e^+, and H^+ each of which could be the major constituent in some altitude region. Since N^+, O_2^+ and NO^+ ions are observed to be always the minor constituents

in the topside ionosphere (Taylor et al., 1968, Taylor, 1971b) they can - to a good approximation - be incorporated individually and a posteriori after a solution for the major constituents has been obtained. The distribution of these minor species is thereby affected by the transport velocities and polarization field of the major ions. Inclusion of N^+ at high latitudes where its concentration can exceed those of the H^+ and He^+ ions (Taylor et al., 1968) and study of the observed longitudinal variations in O_2^+ (Taylor, 1971b) could therefore provide valuable insight into the dynamic properties of the ionosphere.

In the upper ionosphere chemical and local energy processes do not play an important role except near the lower boundaries where the dominance of these processes is utilized to determine the lower boundary conditions. In the lower F and E region where transport processes can be neglected the continuity equations degenerate from differential to algebraic equations, and therefore entirely different solution procedures are appropriate. In this region the ion chemistry is evaluated separately for a multi-constituent plasma including O^+, O_2^+, N_2^+, NO^+ and N^+ (Pharo et al., 1971, Brace et al., 1971).

In describing the density and temperature structure of the protonosphere and its interface with the F_2 region non-local heating (due to escaping photoelectrons) becomes

significant. This has first been pointed out by Geisler and Bowhill (1965). Since this heating mechanism depends on the electron density distribution in a rather complicated way - even with the crude assumptions that are made in this model - a truly simultaneous solution for the mass, momentum and energy equations seems impractical. For this reason the energy equations are solved separately for the plasma temperatures T_e and T_i which are then used in an iterative scheme with the other equations that describe the ion and electron densities. As will be shown, this procedure converges rapidly thus yielding fairly accurate solutions with only a few iterations, and in this way a physically self-consistent solution is obtained.

Since the model presented here treats the ionosphere-protonosphere system as one unit, including the effects of charge exchange and non-local heating, without any ad hoc upper boundary condition, the effects of the ionosphere-protonosphere coupling are obtained in a natural way. The significance of the charge exchange reaction for this coupling was first pointed out by Hanson and Ortenburger (1961)

Finally, the model is designed to describe primarily steady state conditions. However, it has been shown, that this limitation can be removed. A solution for the diurnal variations in the ion composition, involving plasma transport between F_2 region and protonosphere, has been presented by Mayr (1968) and is briefly discussed in Section IV C.

II. Definition and Organization of the Model

In Table I the physical processes, considered in the continuity, momentum, and energy equations, are summarized since they have been discussed in several publications.

Figure 1 shows the organization of the model in the form of a block diagram. Blocks and circles with heavy lines represent processes and internally computed "inputs" respectively, while circles with thin lines represent the true inputs.

Adopting a photon distribution based on Hinteregger et al. (1965) and a model for the gas temperature and neutral composition (Jacchia, 1964), photon absorption is considered and the ionization rates for O^+ and He^+ are computed. At lower heights where chemical reactions dominate, the concentrations of O^+ and He^+ are determined from photochemical equilibrium. This is the case for altitudes up to 180 km for O^+ and up to 400 km for He^+. For H^+ the charge exchange equilibrium relation involving the densities of O^+, O and H is employed up to 400 km. These chemical equilibrium densities serve as the lower boundary conditions for the continuity equations of these constituents.

The charge transfer reaction $O^+ + H \rightarrow H^+ + O$ is the primary source for protons and accordingly the proton content of the magnetosphere is significantly influenced by the concentration of atomic hydrogen at exospheric levels. It had

been postulated for several reasons that bear upon the energetics (Brace et al., 1967) and ion composition (Mayr et al., 1967, Brinton et al., 1969), that the hydrogen concentration should be of the order of 1×10^5/cc at exospheric heights during minimum solar activity. This value which has been used in our model is significantly higher than those in the atmospheric models of Jacchia (1964) and CIRA (1965), but it is consistent with recent results (Brinton and Mayr, 1971a,b) in which for the first time the concentration of atomic hydrogen was deduced from in situ measurements of ion and neutral constituents at around 350 km.

A meridional wind field (described in terms of spherical harmonics by Volland and Mayr, 1968) is adopted as input for the calculation of the neutral-ion drag interaction parallel to the magnetic field. It is assumed that the wind field is defined in the reference frame of geographic latitudes which, to a first order approximation, neglects the feedback effect on the winds due to ion-neutral drag, which is strongly controlled by the geomagnetic field.

The wind field and the plasma distribution are symmetrical with respect to the magnetic equator only if the latitudinal pressure bulge in the neutral atmosphere occurs there. Under this particular condition the transport velocities are zero at the equator. This condition determines the solution of the continuity equations uniquely. When the bulge is not at the geomagnetic equator, the wind velocities are different in the northern and southern hemispheres along a particular field line, thus inducing asymmetries in the plasma distribution

with respect to the magnetic equator. Such asymmetries are associated with plasma transport across the equator which has to be considered in a self-consistent way in order to find unique solutions.

The scheme in which these transport fluxes are incorporated is briefly the following: For the hemisphere in which the plasma densities are higher on outward flow of the major ion component (normally H^+ at the equator) is introduced and its equatorial density is computed for a number of flux values. For the same value inward flows into the field tube of the other hemisphere are then used to compute the corresponding equatorial densities. From the condition that equatorial densities must be equal, the inter-hemispheric transport flux for the major constituent is then determined. Similar procedures are applied for the minor constituents so that eventually the various transport fluxes satisfy the upper boundary condition of continuous density transition across the equator for all ion species.

The plasma temperatures T_e and T_i are initially assumed equal to the gas temperature to start the solution for the equations of mass and momentum conservation. The resulting electron density distribution, N_e, is then used to compute the non-local heating rate due to escaping photoelectrons. The calculation of the local and non-local heating rates has been based on the method of Fontheim et al. (1968).

With these heating rates and the electron-ion, electron-neutral, and ion-neutral loss rates, the energy equations are solved for the electron and ion temperatures. The boundary conditions are obtained by assuming local energy equilibrium (neglect of heat conduction) at lower altitudes and zero heat flux at the equator under conditions where the plasma distribution can be assumed to be symmetrical with respect to the magnetic equator. Under conditions of plasma density asymmetry a symmetric temperature distribution has been adopted to study the effects of inter-hemispheric mass transport. The effects of inter-hemispheric energy transport have not been treated so far but they can, of course, be incorporated into the model.

The resulting temperature distributions are then fed back into the momentum and continuity equations, and the iteration (including the electron density dependent heating rates) is continued until the relative differences between successive density and temperature values become smaller than a few percent throughout the entire altitude range. This procedure converges very rapidly, and it is found that four to five iterations are usually sufficient to produce fairly accurate solutions.

In this iterative cycle the calculation of the heating rates must be performed three to four times. The computation time for this calculation exceeds by far the total computation time for the solution of the continuity and energy equations.

In the latitudinal temperature study reported in Section IV B a simplified heat input model has therefore been used. By assuming a monoenergetic beam of photoelectrons of typically 10 ev (corresponding to the maximum in the photoelectron spectrum (Fontheim et al., 1968)) and with zero pitch angle the non-local heat input is calculated from the Coulomb loss rate given by Butler and Buckingham (1962) and Dalgarno et al. (1963). The local heat input is assumed to be proportional to the atmospheric density with the proportionality factor as an input parameter based on the heating rates of Fontheim et al. (1968).

Although thermal diffusion (Walker, 1967) has not been considered in the model calculations presented in Section IV, it is included in the present version of the model.

III. Solution Procedure

The procedure for solving the momentum and continuity equations is outlined for a two constituent plasma of O^+ and H^+ ions. The continuity and momentum equations have the form

$$Q - L\,[O^+] - B\,\frac{\partial}{\partial s}\left(\frac{[O^+]\,V_{O^+}}{B}\right) = \frac{\partial\,[O^+]}{\partial t}, \qquad (1)$$

$$K_1\,[O^+]\,[H] - K_2\,[H^+]\,[O] - B\,\frac{\partial}{\partial s}\left(\frac{[H^+]\,V_{H^+}}{B}\right) = \frac{\partial\,[H^+]}{\partial t}, \qquad (2)$$

$$\theta_{O^+N}\,[O^+]\,[N]\,(V_{O^+}-V_{\parallel}) + \theta_{O^+H^+}\,[O^+]\,[H^+]\,(V_{O^+}-V_{H^+})$$

$$+ m_{O^+} V_{O^+} \frac{\partial V_{O^+}}{\partial s}[O^+] = -k\,T_i \frac{\partial [O^+]}{\partial s} - k\,[O^+]\,\frac{\partial T_i}{\partial s} \qquad (3)$$

$$- m_{O^+}\,g_{\parallel}\,[O^+] - \frac{k\,T_e}{N_e}\,\frac{\partial N_e}{\partial s}\,[O^+] - k\,\frac{\partial T_e}{\partial s}\,[O^+],$$

$$\theta_{H^+N}\,[H^+]\,[N]\,(V_{H^+}-V_{\parallel}) + \theta_{O^+H^+}\,[O^+]\,[H^+]\,(V_{O^+}-V_{H^+})$$

$$+ m_{H^+} V_{H^+} \frac{\partial V_{H^+}}{\partial s}[H^+] = -k\,T_i \frac{\partial [H^+]}{\partial s} - k\,[H^+]\,\frac{\partial T_i}{\partial s} \qquad (4)$$

$$- m_{H^+}\,g_{\parallel}\,[H^+] - \frac{k\,T_e}{N_e}\,\frac{\partial N_e}{\partial s}\,[H^+] - k\,\frac{\partial T_e}{\partial s}\,[H^+],$$

where $N_e = [O^+] + [H^+]$

$[O^+]$, $[H^+]$ = concentrations of O^+, H^+

s = distance along a field line

Q = photoionization rate for O^+

L = O^+ loss rate for charge transfer and ion molecule reactions with O_2 and N_2 (function of the concentrations of H, O_2, and N_2)

$B = \frac{M}{r^3}\,(1 + 3\cos^2\theta)^{1/2}$

M = magnetic dipole moment of the earth

r = geocentric radius

θ = geomagnetic (dipole) latitude

t = universal time

V_{O^+}, V_{H^+} = transport velocities of O^+, H^+

κ_1, κ_2 = charge transfer coefficients

$v_{\parallel}$ = meridional wind component parallel to the magnetic field

$[N]$ = concentration of the neutral atmosphere

$\theta_{O^+H^+}$ = drag coefficient for momentum transfer between O^+ and H^+

θ_{O^+N}, θ_{H^+N} = drag coefficient for momentum transfer between O^+, H^+ and N

T_e, T_i = electron and ion temperatures

m_{O^+}, m_{H^+} = masses of O^+, H^+ ions

$g_{\parallel}$ = gravitational acceleration parallel to the magnetic field

k = Boltzmann's constant

After formally integrating equations (1) and (2) one obtains the following expressions for the transport velocities

$$V_{o^+} = \frac{B}{B_e} \frac{j_{o^+e}}{[O^+]} - B \int_S^{S_e} \left\{ Q - L\,[O^+] - \frac{\partial\,[O^+]}{\partial\,t} \right\} d\,s, \qquad (5)$$

$$V_{H^+} = \frac{B}{B_e} \frac{j_{H^+e}}{[H^+]} - B \int_s^{s_e} \left\{ K_1\,[O^+]\,[H] - K_2\,[H^+]\,[O] - \frac{\partial\,[H^+]}{\partial\,t} \right\} d\,s \qquad (6)$$

where j_{O^+} and j_{H^+} refer to particle fluxes and the subscript e denotes the values of the functions at the equator.

If the left hand sides of Equations (3) and (4) are formally denoted by $[O^+]\ D_{O^+}([O^+], [H^+], j_{O^+}, j_{H^+})$ and $[H^+]\ D_{H^+}([O^+], [H^+], j_{O^+}, j_{H^+})$, the momentum equations take the form of homogeneous equations

$$k T_i \frac{\partial [O^+]}{\partial s} + \left\{ k \left(\frac{\partial T_e}{\partial s} + \frac{\partial T_i}{\partial s} \right) + \frac{k T_e}{N_e} \frac{\partial N_e}{\partial s} + m_{O^+} g_{\parallel} + D_{O^+} \right\} [O^+] = 0, \tag{7}$$

$$k T_i \frac{\partial [H^+]}{\partial s} + \left\{ k \left(\frac{\partial T_e}{\partial s} + \frac{\partial T_i}{\partial s} \right) + \frac{k T_e}{N_e} \frac{\partial N_e}{\partial s} + m_{H^+} g_{\parallel} + D_{H^+} \right\} [H^+] = 0, \tag{8}$$

which can be integrated to describe the density distributions in the form

$$[O^+] = [O^+]_0 \exp \left\{ - \int_{s_0}^{s} \left[\frac{m_{O^+} g_{\parallel}}{k T_i} + \frac{1}{T_i} \frac{\partial}{\partial s} (T_e + T_i) + \frac{T_e}{T_i} \frac{\partial}{\partial s} \ln N_e + D_{O^+} \right] d s \right\}, \tag{9}$$

$$[H^+] = [H^+]_0 \exp \left\{ - \left[\int_{s_0}^{s} \frac{m_{H^+} g_{\parallel}}{k T_i} + \frac{1}{T_i} \frac{\partial}{\partial s} (T_e + T_i) + \frac{T_e}{T_i} \frac{\partial}{\partial s} \ln N_e + D_{H^+} \right] d s \right\}, \tag{10}$$

where $[O^+]_o$ and $[H^+]_o$ are the lower boundary conditions. Since D_O+ and D_H+ are integral functions of the densities $[O^+]$ and $[H^+]$, the equations (9) and (10) are integral equations. The solution of these equations is accomplished by means of an iterative procedure in which the functions D_O+ and D_H+ are treated as perturbations in the following scheme. For the kth iteration the perturbation functions are

$$D_O^k+ = \varepsilon_k \, D_O^{k-1}+$$

$$D_H^k+ = \varepsilon_k \, D_H^{k-1}+$$

where ε_k is a parameter that is assumed to vary between

$$0 \leq \varepsilon_{k-1} < \varepsilon_k < \varepsilon_{k+1} \leq 1.$$

For the initial solution we assume $\varepsilon_1 = 0$ which is equivalent to diffusive equilibrium. In subsequent iterations ε_k is gradually increased to allow the perturbation function to become effective slowly. This procedure assures the applicability of the perturbation method which demands small effects from the "perturbing" function. A successive application of this procedure leads to a convergence to the solution of equations (9) and (10) when ε_k approaches 1.

These solution procedures can be directly extended to incorporate He^+ ions. Figure 2 shows the results of a sample calculation of composition profiles including He^+.

For the time-dependent case ($\frac{\partial}{\partial t} \neq 0$) this scheme is extended by substituting for the kth iteration

$$\left(\frac{\partial [O^+]}{\partial t}\right)_k = \epsilon_k \left(\frac{\partial [O^+]}{\partial t}\right)_{k-1}$$

$$\left(\frac{\partial [H^+]}{\partial t}\right)_k = \epsilon_k \left(\frac{\partial [H^+]}{\partial t}\right)_{k-1}$$

In the initial solution it is assumed that $\epsilon_1 = 0$ corresponding to steady state. The density distributions are computed in time intervals of 1 hour to generate the quasi-stationary diurnal variation under the influence of the diurnal variations of the O^+ and H^+ boundary conditions, the solar flux, and the neutral atmosphere. In subsequent iterations ϵ_k is then increased toward 1 to produce finally the time-dependent solution.

The energy equations for T_e and T_i have the form

$$\frac{2}{7} K_e B \frac{\partial}{\partial s}\left(\frac{1}{B} \frac{\partial}{\partial s} T_e^{7/2}\right) = Q_e - K_{ei} (T_e - T_i) - K_{en} (T_e - T_n), \quad (12)$$

$$K_{ei} (T_e - T_i) = K_{in} (T_i - T_n), \quad (13)$$

where

κ_e = heat conduction coefficient for electrons

Q_e = heating rate for electrons (dependent on electron and neutral densities)

K_{ei}, K_{en}, K_{in} = rate coefficients for energy loss between the various electron, ion and neutral constituents thus depending on their densities.

Equation (12) can be formally integrated to yield

$$T_e(s) = \left\{ T_{e0}^{7/2} + \frac{7}{2K_e} \int_{s_0}^{s} \left[\frac{B}{B_e} j_e + B \int_{s_e}^{s'} \frac{1}{B} (Q_e - K_{ei}(T_e - T_i) - K_{en}(T_e - T_n)) \, ds \right] ds' \right\}^{2/7} \tag{14}$$

with

T_{e_o} = lower boundary condition, computed from local energy equilibrium

j_e = heat flux across the equator normally assumed to be zero.

The integral equation (14) is solved iteratively by increasing ε from 0 to 1, in a similar way as has been described for the solution of the ion continuity equations.

In the following a few model studies are presented which demonstrate some of the dynamic and energetic characteristics of the upper ionosphere.

IV. Discussion

A) The Effects of Interhemispheric Plasma Transport Bearing on Longitudinal Variations in the Ionosphere.

For illustration we shall consider wind effects originally introduced by King and Kohl (1965) during equinox to produce a condition of asymmetry. It is assumed that the meridional

wind velocity is zero at the subsolar point which in turn occurs at the geographic equator. Following Volland and Mayr (1968) the wind field is then described in terms of spherical harmonics of low degrees

$$v = v_{10} P_{10} \cos \theta + v_{21} \frac{P_{21}}{\cos \theta} \cos [\omega (\tau - \tau_{21})], \qquad (15)$$

where

$P_{10} = \sin \theta_g$

$P_{21} = \frac{3}{2} \sin 2 \theta_g$

θ_g = geographic latitude

$\tau = t + \lambda/\omega$ (local time)

t = universal time

$\omega = 2\pi/ \tau_o$ (angular frequency with τ_o the period of one day

λ = geographic longitude

τ_{21} = 1400 local time (time of the observed diurnal maximum in the atmospheric density)

v = meridional wind velocity

Assuming that the altitudinal variations of v within the F_2 region are small compared with the variations in the neutral density and therefore negligible, Equation (15) is defined with two parameters v_{10} and v_{21}, which according to Volland and Mayr (1968) are assumed to be of the order of v_{10} = 10 m/sec and v_{21} = 50 m/sec.

It is the wind component parallel to the magnetic field which enters into the ion continuity equations. The wind field in (15) must therefore be described as a function of geomagnetic latitude. This is straightforward for the two longitudes in which the earth's axis of rotation, the magnetic dipole vector, and the earth-sun-line lie in the same plane. At American longitudes the magnetic equator is south of the geographic equator, and thus the wind field can be described by substituting in Equation (15) $\theta = \theta_g + 12°$, where θ is the geomagnetic latitude. This then exhibits explicitly the asymmetry of the wind field with respect to the magnetic equator. The downward wind component in the southern hemisphere is larger by almost a factor of two than in the northern hemisphere at about 30° geomagnetic latitude.

With this wind field the ion composition has been computed along the field line with L = 1.4 which corresponds to about $\pm$30° latitude at F_2 region heights. Figure 3 shows the results, on the left hand side for the northern hemisphere and on the right hand side for the southern hemisphere. It is apparent that in the northern hemisphere (left) the F_2 peak density is larger and occurs at a higher altitude than in the southern hemisphere (right), thus reflecting the difference in the wind velocities. The larger downward wind component thereby drags the F_2 region ionization (O^+) to lower heights where the increase in the recombination rate causes the ion density to decrease.

The dotted lines show the ion distributions for O^+ and H^+ which were computed assuming zero plasma transport across the equator. As a result it is seen in Figure 3 that the equatorial H^+ concentration is by about a factor of five larger in the northern hemisphere than in the southern hemisphere. Such a discontinuity across the equatorial plane is of course unrealistic. Therefore H^+ fluxes are introduced across the equatorial plane from the northern to the southern hemisphere in a scheme that has been described in Section II.

In this case an H^+ flux of $5.4 \times 10^7/cm^2$ sec is required to match the H^+ densities from both hemispheres at the equator. The resulting electron and H^+ distributions are shown in solid lines. The O^+ distribution is represented by the dashed line which coincides with the solid line at lower altitudes. It is apparent from this that the interhemispheric plasma transport, induced by the asymmetry in the thermospheric wind field, decreases the protonospheric density by about a factor of two in the northern hemisphere thus raising the O^+-H^+ transition level by 90 km while it increases the proton density in the southern hemisphere and accordingly lowers the O^+-H^+ transition level by 70 km. The effect of this interhemispheric plasma transport is also seen in the scale height of the O^+ concentration within the F_2 region. At these altitudes the H^+ flux is about $10^8/cm^2$sec an increase by a factor of 2 from the equatorial value due to the convergence of the field tube. The H^+-O^+ drag resulting from this upward proton flux in the northern hemisphere causes an increase in the O^+

scale height above the region where H^+ is in chemical equilibrium (up to about 500 km). Conversely in the southern hemisphere the downward flux decreases the O^+ scale height. Below 500 km where H^+ becomes chemically controlled, the ionization transport is taken over from H^+ to O^+ ions thus producing O^+ fluxes of the order of 10^8 above the F_2 peak. These fluxes therefore eventually influence the height and density of the F_2 peak, though only slightly.

Up to this point only interhemispheric plasma transport by protons has been considered. Under this condition the O^+ density is still discontinuous across the equator as is apparent from Figure 3 in which the O^+ density distribution is shown as a dashed line above 1400 km. It is apparent that, with the H^+ flux alone, the O^+ densities from both hemispheres differ by more than a factor of 10 at the equator. However, after the introduction of O^+ fluxes, the density continuity in O^+ is established with a flux of $5.1 \times 10^5/cm^2 sec$. The resulting density distributions are shown in solid lines in Figure 3. The effect of this O^+ flux is negligible for the H^+ distribution, and it affects O^+ only above 1600 km as is evident from the deviation between the dashed and the solid lines in Figure 3. It is apparent from this that in the northern hemisphere, where the F_2 region densities are higher, the O^+ scale height decreases significantly above 2000 km, while in the southern hemisphere, where O^+ is supplied, the concentration of O^+ even increases with height. This somewhat peculiar distribution

thereby indicates that the minimum in the O^+ density is shifted from the equator toward the southern hemisphere which is quite plausible considering that the F_2 region ionization is also lower there.

At other longitudes, and in particular at European and Asian longitudes, the asymmetry in the ion density distributions between the southern and northern hemispheres would be opposite to the case discussed here. As has been shown by Brinton et al., (1970), this effect can account for significant longitudinal variations in the O^+-H^+ transition level. Taylor et al., (1970) and Taylor (1971a) have presented comprehensive evidence for the solar geomagnetic control of the ion composition from OGO 4 and 6 ion mass spectrometer measurements thus demonstrating that the longitudinal variations - which bear upon the effects discussed here - are very significant and are comparable in magnitude with the latitudinal and local time variations in the ion composition (Taylor, 1971b).

B) Latitudinal Electron Temperature Variation

Equations (5), (6), (9), (10), (12) and (13) have been solved for several latitudes under equinox conditions (zero flux across the equatorial plane) to study the latitudinal variations in the electron temperature (see for details also Mayr et al., 1968). In Figure 4 the electron temperature is shown as a function of geomagnetic latitude for several altitudes. For comparison, the observed latitudinal temperature distribution at 1000 km (Brace et al., 1967) is also presented. The agreement between the measured

and calculated temperatures is excellent up to 60° geomagnetic latitude. In particular, the calculated profiles clearly show the equatorial trough and the maximum at mid-latitude. Above 60°, at the plasmapause and beyond, H^+ is depleted by electric field convection and polar wind escape. This mechanism is not included in our equations, and therefore the disagreement with experiment above 60° is to be expected.

To provide some insight into the physical mechanisms which determine the downward heat flow at 1000 km the various integrated energy rates are shown in Figure 5. The dashed line shows the energy input due to fast electrons, the dash-dotted line shows the energy loss between plasma and neutral atmosphere, and the solid line represents the difference between input and loss, which represents the heat flux at 1000 km.

The latitudinal variation of the energy input above 1000 km depends strongly on the rate at which the photoelectrons lose their energy at lower altitudes. Near the equator, the electron density is high, and almost all of the energy is absorbed below 1000 km. Thus only a small amount of energy can heat the ionosphere above this height. With increasing latitude the electron density decreases, and an increasingly larger fraction of the energy becomes available as input at higher altitudes. Above 40° the latitudinal variation in the electron density is small, and therefore the energy input above 1000 km stays constant.

The total rate of energy loss due to collisions in field tubes above 1000 km (also shown in Figure 5) depends proportionally on the ion content and on the density of the neutral atmosphere (primarily neutral hydrogen). Additionally, the loss rate is a function of the ion and neutral species involved in this loss process. Hydrogen ions lose their energy most effectively to hydrogen atoms, and similarly oxygen ions cool most rapidly to neutral oxygen but at a rate 4 times lower than the loss rate between H^+ and H (Brace et al., 1965). At the equator, the loss rate is small because of the small field tubes and their small particle population. With increasing latitude the field tube volume increases and so does the total ion content. The result is an increase of the energy loss rate. Between 20° and 40° latitude the ion content increases further, and there is a small increase in the population of neutral particles. But simultaneously the mean ion mass increases thus decreasing the effectiveness of the cooling process. The net result is that the loss rate changes little with latitude. At latitudes above 40° the field tube volumes strongly increase and therefore the contact between plasma and neutral atmosphere involves significantly larger particle populations. The net effect is that the integrated loss rate rapidly increases at higher latitudes.

The variation of the heat flux (solid line in Figure 5) reflects the very different behavior of input and loss rates with latitudes. Near the equator both energy input and loss

rates are low. The loss exceeds the gain, and this requires a negative temperature gradient along field lines that contributes to the low equatorial temperature. Up to middle latitudes the energy input increases while the loss function changes little. Therefore the heat flux increases as does the temperature. Above 40° the energy loss starts to increase and the input levels off. Thus the heat flux forms a maximum at 50° where T_e is also highest. Beyond this latitude the energy loss rate rises rapidly with latitude. This leads to a rapid decrease of the heat flux and to a similar decrease of the temperature at high latitudes.

Figure 4 shows that at high latitudes (above 60°), the calculated temperatures decrease significantly below the measured ones. The reason for this discrepancy may be that some of the assumptions in our model are not valid at high latitudes. For example, electric fields which would give rise to Joule heating may play an important role outside the plasmasphere; yet their effects have not been included nor have we considered the effects of precipitating electrons in the present model (Paulikas, 1971; Fontheim et al., 1971a; Fontheim et al., 1971b).

The ion composition which was simultaneously computed with the electron temperature was used to determine the mean ion mass, m^+, at 1000 km. It is shown in Figure 6 in comparison with results deduced from OGO 2 (Taylor et al., 1968). The agreement is good up to middle latitudes. However above 50°, where the discrepancy in the temperature becomes apparent, the observed mean ion mass increases to its maximum value of

16 AMU, whereas the computed values of m^+ decrease to 3 AMU. This means that in our model the electron density scale height is too high by a factor of 5 and consequently the total ion content above 1000 km is also too high. This discrepancy has been interpreted as due to a continuous upward flux of protons that increases the mean ion mass and raises the O^+-H^+ transition level (Mayr et al., 1967) thus masking at these high latitudes the diurnal redistribution between ionosphere and protonosphere (Mayr, 1968). These fluxes which have also been inferred from the ion distributions across the plasmapause (Taylor et al., 1969, Mayr et al., 1970a, Brinton et al., 1971) are associated with electric field convection (Nishida, 1966), and polar wind escape (Banks and Holzer, 1968).

As shown earlier, the integrated collisional energy loss rate is very sensitive to the total plasma content in the field tube and to the mean ion mass. A reduction of the proton content would lead to a reduction in the integrated energy loss rate, and this, in turn, would tend to increase the temperature. A significant reduction in the proton content would also cause the protonosphere to become transparent to photoelectrons and as a consequence the heat input into the protonosphere would decrease as well. Most of the photoelectron energy could therefore be dissipated in the conjugate hemisphere thus heating primarily the plasma below 1000 km which in turn would reflect upon the temperature at this height level.

Hence, the discrepancies between the calculated and measured composition and temperatures at high latitudes could - though in a rather complicated manner - be related to the same physical mechanism, the loss of plasma outside the plasmasphere.

C) Discussion of Time-Dependent Solutions

The time-dependent equations are solved iteratively as has been discussed in Section III (for details see Mayr, 1968). In this way the problem is again reduced to a boundary value problem. At the lower boundary (300 km) the temporal variation of $[O^+]$ is assumed to be of the form

$$[O^+] = [O^+]_0 + [O^+]_1 \sin \frac{2\pi}{\tau_0} t, \qquad (16)$$

where τ_o is the period of one day. H^+ is assumed to be in chemical equilibrium through charge exchange, and its density at the boundary is therefore given by the expression

$$[H^+] = \frac{9}{8} \frac{[O^+]\ [H]}{[O]}. \qquad (17)$$

The neutral densities [O] and [H] at 300 km are assumed to be given by an expression of the form (16) and so are the neutral and charged particle temperatures. The ion and electron temperatures are assumed to be equal and to be constant with altitude.

Calculations have been performed along a midlatitude

Table II lists the values of the input parameters. In Figures 7 through 9 the time-dependent solutions (solid curves) for O^+, H^+, and electrons are compared with the quasi-stationary solutions ($\partial/\partial t = 0$) (dashed curves). It is immediately evident that the differences between the time-dependent and stationary solutions are significant (especially at high altitudes), and thus the steady state assumption is not always appropriate in describing the topside ionosphere.

The O^+ concentration (Figure 7) exhibits a noon maximum at all altitudes. Since the same lower boundary condition is being used for the steady state and time-dependent cases, the solutions hardly differ at lower altitudes. With increasing altitude the effect of the boundary condition becomes less important, and therefore the time-dependent and stationary solutions start to deviate.

The H^+ density (Figure 8) shows a significantly more complex behavior. At 300 km its peak is in phase with O^+, and its minimum stretches over several hours during the night. This is a consequence of the ion chemistry that involves variations of O^+, O, and H. At 500 km, however, the temporal behavior of H^+ shows a radically different picture. A broad minimum at daytime is followed by a sharp maximum during the night. The reason for this change can again be found in the ion chemistry which at this altitude involves significantly different [O]/[H] ratios. In addition it is evident from the difference between the stationary and time dependent solutions that downward fluxes of H^+ enhance the

proton concentration at night by almost a factor of two. At 700 km the temporal variations of H^+ result from the interaction of several mechanisms. At this altitude the transition from the F_2 region to the protonosphere occurs which means for H^+ that transport processes start to dominate chemical processes. This is apparent from the large differences between the stationary and time dependent solutions which show that during daytime upward fluxes decrease the H^+ concentration while at night downward fluxes enhance the H^+ concentration. These features prevail up to about 2500 km where the H^+ density is decreased during the day and enhanced at night such that the amplitude of the temporal variation is lowered by a factor of two and the phase is shifted by almost three hours. The diurnal behavior of O^+ and H^+ discussed above is in essential agreement with the measurements of Brinton et al., (1969).

The dynamic effects are exhibited best by the electron density distribution (Figure 9). It shows that with increasing altitude the amplitude decreases while density minima and maxima shift in time. These effects occur at night above 500 km and at daytime above 700 km, the reason being that the O^+-H^+ transition region is at a lower altitude at night than it is during daytime.

In Figure 10 the altitude of the O^+-H^+ transition level in the time-dependent case is compared with that for the steady state case. The difference is very pronounced showing that dynamic effects raise the transition level during

the day by 150 km and lower it at night by 100 km. Thus the amplitude of the variation of the transition level increases as the result of dynamic effects, which give rise to upward fluxes of plasma during the day and downward fluxes at night. The nighttime downward flux has also been predicted by Nagy et al., (1968). In general, the daytime upward flux of H^+ above the transition level is sustained by an upward flux of O^+ between the F_2 region and the transition level. At night, of course, the flows are reversed. This diurnal variation of the O^+ flux has been observed by Evans (1971) and by Carpenter and Bowhill (1971).

V. Summary and Conclusion

The ionosphere-protonosphere system is governed by many interlocking mechanisms. Some of these are chemical reactions (including ionization and recombination), transport of both mass and energy, energy input, and energy loss. In addition, the neutral atmosphere interacts with the ionosphere and is in turn modified by it. The various mechanisms are determined by cross sections, rate, and transport coefficients most of which are not very accurately known. In setting up the equations describing the ionosphere-protonosphere system it is, therefore, neither practical nor physically meaningful to write them in their most general form. Fortunately, not all of the mechanisms are of equal importance everywhere. Significant simplifications can, therefore, be achieved by restricting a given model to a certain range in altitude or latitude or both.

The equations discussed above apply to the ionosphere at low and midlatitudes (inside the plasmasphere) above the F region. Therefore the equations involve only three constituents, O^+, H^+ and He^+

The emphasis in this treatment is on the dynamic effects. It is, therefore,of special importance to eliminate, as far as possible, any arbitrariness, arising out of the uncertainties in the boundary conditions. The lower boundary conditions are determined by utilizing the predominance of local chemical processes below the F region. The equations are integrated from both hemispheres up to the magnetic equatorial plane. If the neutral wind fields are asymmetric with respect to the equatorial plane, they give rise to asymmetric ion density profiles. In that case interhemispheric ion fluxes are introduced in a self-consistent way by requiring continuity of all physical parameters across the equatorial plane. These continuity requirements are the upper boundary conditions.

The energy equations for T_e and T_i are solved separately in an iteration in series with the continuity and momentum equations. This scheme facilitates the inclusion of non-local heating which depends on the density distribution of the ambient plasma.

Some of the conclusions drawn from the case studies presented here are summarized below:

1) Even under steady state conditions the ion transport fluxes induced by wind generated asymmetries in the plasma population are significant and thus affect

considerably the O^+-H^+ transition level and the scale heights of all ion species. In general, the assumption of diffusive equilibrium does therefore not hold, not even for the major ion constituents.

2) The latitudinal variation of electron temperatures at 1000 km is shown to be related to the processes of non-local heating and collisional energy loss both of which depend in a complex way on the electron and ion distributions within each particular field tube.

3) If the time dependence is taken into account, the diurnal plasma exchange between the F_2 region and the protonosphere is shown to be significant thus affecting considerably the diurnal amplitude of both the O^+-H^+ transition level and the protonospheric density content.

Acknowledgment

One of the authors (EGF) gratefully acknowledges support of his work by the U. S. National Aeronautics and Space Administration through grant No. NGR-23-005-015. The authors are indebted to R. S. Stolarski for having provided them with all of the electron impact cross sections and to H. Volland for many valuable discussions.

References

Banks P. M. and Holzer T. E. 1968 J. Geophys. Res. 73, 6846

Brace L. H., Spencer N. W., and Dalgarno A. 1965 Planet. Space Sci. 13, 647

Brace L. H., Reddy B. M., and Mayr H. G. 1967 J. Geophys. Res. 72, 265

Brace L. H., Mayr H. G., and Findlay J. A. 1969 J. Geophys. Res. 74, 2952

Brace L. H., Mayr H. G., and Mahajan K. K. 1970 J. Atm. Terr. Phys. 32, 1945

Brinton H. C., Pharo, M.W. III, Mayr H. G., and Taylor H. A. Jr. 1969 J. Geophys. Res. 74, 2941

Brinton H. C., Mayr H. G., Pickett R. A., and Taylor H. A. Jr. 1970 Space Research X, 652

Brinton H. C., Grebowsky J. M., and Mayr H. G. 1971 J. Geophys. Res. 76, 3738

Brinton H. C. and Mayr H. G. 1971a J. Geophys. Res. 76, 6198

Butler S. T. and Buckingham M. J. 1962 Phys. Rev. 126, 1

Carpenter L. A. and Bowhill S. A. 1971 Trans. Am. Geophys. U. 52, 301

CIRA, Cospar International Reference Atmosphere 1965 North-Holland Publ. Co., Amsterdam

Dalgarno A., McElroy M. B., and Moffett R. J. 1963 Planet. Space Sci. 11, 463

Evans J. V. 1971 Radio Sci. 6, 609

Fontheim E. G., Beutler A. E., and Nagy A. F. 1968 Ann. Geophys. 24, 489

Fontheim E. G., Lyzenga D. R., Brace L. H., Mayr H. G., and Heikkila W. J. 1971a Trans. Am. Geophys. U. 52, 305

Geisler J. E. and Bowhill S. A. 1965 J. Atm. Terr. Phys. 27, 1119

Hanson W. B. and Ortenburger J. B. 1961 J. Geophys. Res. 66, 1425

Hinteregger H. E., Hall L. A., and Schmidtke J. 1965 Space Res. V, 1175

Jacchia, L. G. 1964 Smithsonian Inst. Astrophys. Obs., Special Report No. 170

King J. W. and Kohl H. 1965 Nature 206, 699

Mayr H. G., Brace L. H., and Dunham G. S. 1967 J. Geophys. Res. 72, 4391

Mayr H. G. and Brace L. H. 1970 J. Geophys. Res. 75, 2608

Mayr H. G. Grebowsky J. M., and Taylor H. A. Jr. 1970a Planet. Space Sci. 18, 1123

Mayr H. G., Taylor H. A. Jr., and Brinton H. C. 1970b Trans. Am. Geophys. U. 51, 373

Nagy A. F., Bauer P., and Fontheim E. G. 1968 J. Geophys. Res. 73, 6259

Nishida A. 1966 J. Geophys. Res. 71, 5669

Paulikas G. A. 1971 Rev. Geophys. and Space Phys. 9, 659

Pharo M. W. III, Scott L. R., Mayr H. G., Brace L. H., and Taylor H. A. Jr. 1971 Planet Space Sci. 19, 15

Taylor H. A. Jr. 1971a Planet. Space Sci. 19, 77

Taylor H. A. Jr., Brinton H. C., Pharo M. W. III., and Rahman N. K. 1968 J. Geophys. Res. 73, 5521

Taylor H. A. Jr., Brinton H. C., Carpenter D. L., Bonner F. M., Heyborne R. L. 1969 J. Geophys. Res. 74, 3517

Taylor H. A. Jr., Mayr H. G., and Brinton H. C. 1970 Space Res. X, 663

Walker J. C. G. 1967 Planet. Space Sci. 15, 1151

Reference is also made to the following unpublished material:

Brace L. H., Mayr H. G., Pharo M. W. III, Scott L. R., Spencer N. W. and Carignan G. R. 1971 The electron heating rate and ion chemistry in the thermosphere above Wallops Island during the solar eclipse of March 7, 1970. Presented at COSPAR in Seattle, Washington, June 1971. Also: Goddard Space Flight Center Report No. X-621-71-273

Brinton H. C. and Mayr H. G. 1971b Thermospheric hydrogen: Absolute densities and temporal variations deduced from in situ measurements. Space Research XII, in press.

[illegible]heim E. G., Mayr H. G., Brace L. H., Jackson J. E., and Heikkila W. J. 1971b Effect of particle precipitation during a magnet[illegible]pheric substorm. Presented at the Symposium on Magnetospheric Substorms held in conjunction with the XVth General Assembly of the International Union of Geodesy and Geophysics in Moscow, August 2-13, 1971

Mayr H. G. 1968 The dynamic coupling between F_2 region and protonosphere. Goddard Space Flight Center Report No. X-621-68-444

Mayr H. G., Brace L. H., and Crevier W. 1968 The latitudinal temperature structure of the topside ionosphere. Presented at the URSI Spring Meeting, Washington, D. C., April, 1968. Also: Goddard Space Flight Center Report No. X-621-68-233

Taylor H. A. Jr. 1971b Observed solar geomagnetic control of the ionosphere: Implications for reference ionospheres. Goddard Space Flight Center Report No. X-621-71-232

Volland H. and Mayr H. G. 1968 On the diurnal tide within the thermosphere. Goddard Space Flight Center Report No. X-621-68-444

Table I

Physical Processes

1) Photoionization

$O + h\upsilon \rightarrow O^+ + e$

$He + h\upsilon \rightarrow He^+ + e$

2) Charge transfer and ion molecule reactions

$O^+ + O_2 \rightarrow O_2^+ + O$

$O^+ + N_2 \rightarrow NO^+ + N$

$H^+ + O \underset{\leftarrow}{\rightarrow} O^+ + H$

$He^+ + N_2 \rightarrow N_2^+ + He$

3) Drag (diffusive) interactions between the various ion species

4) Drag interaction between neutral and ion species, considering the meridional wind component along field lines

5) Collisional energy loss processes between the various charged and neutral constituents

6) Thermal heat conduction in the electron component; ion heat conduction is neglected

7) Local and non-local heating

8) Interhemispheric transport of plasma under conditions of seasonal asymmetry

Table II

List of Input Parameters for Time-Dependent Case

$[O^+]_0 = 2.0 \times 10^5 cm^{-3}$	$[O^+]_1 = 5.0 \times 10^4 cm^{-3}$
$[O]_0 = 1.5 \times 10^7 cm^{-3}$	$[O]_1 = 1.0 \times 10^7 cm^{-3}$
$[H]_0 = 2.0 \times 10^5 cm^{-3}$	$[H]_1 = 2.0 \times 10^4 cm^{-3}$
$T_0 = 2.0 \times 10^3 °K$	$T_1 = 5.0 \times 10^2 °K$
$T_{n0} = 1.0 \times 10^3 °K$	$T_{n1} = 2.0 \times 10^2 °K$

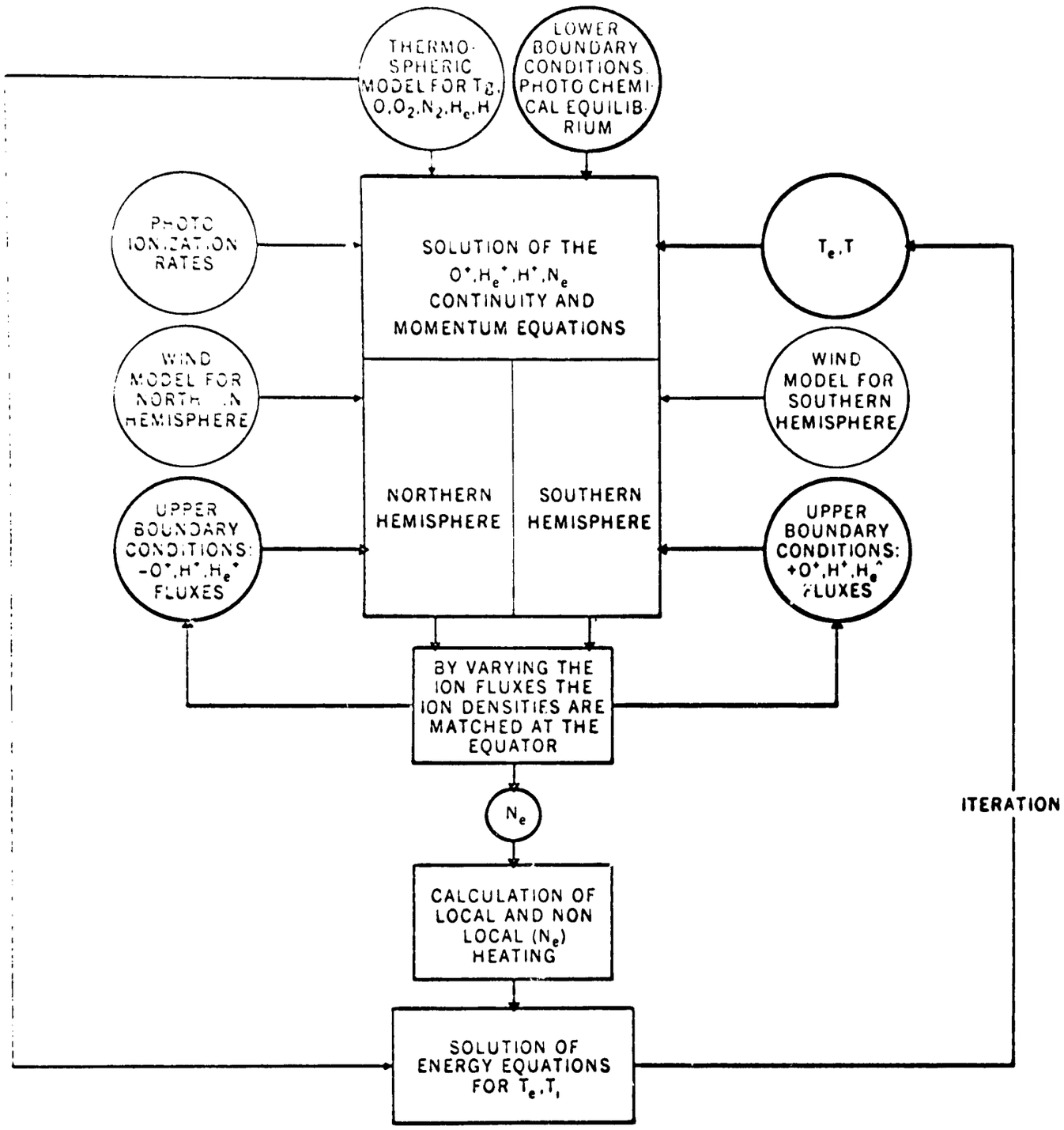

Figure 1. Organization of the ionosphere model.

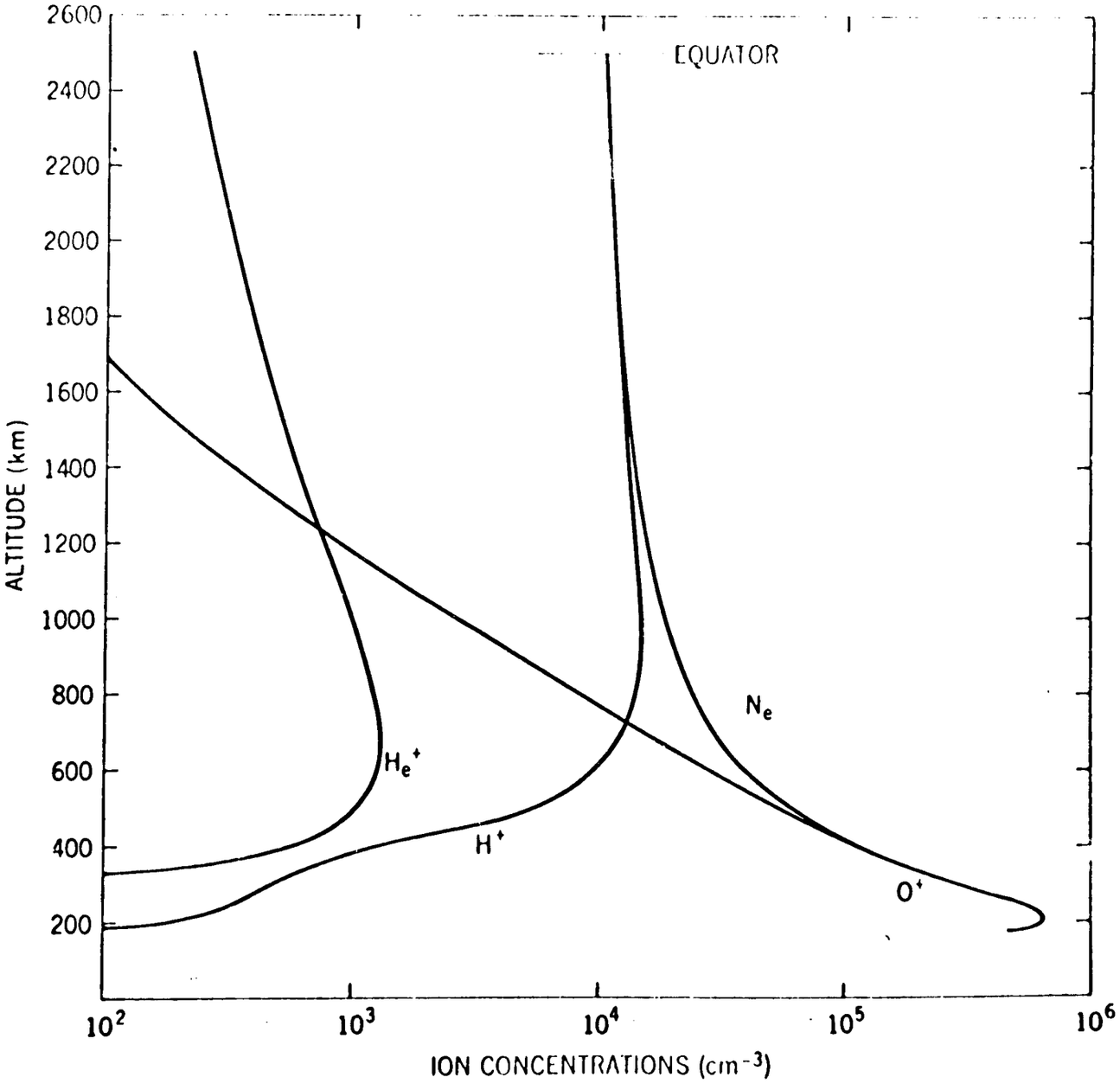

Figure 2. Calculated composition profiles of O^+, H^+, He^+, and electrons.

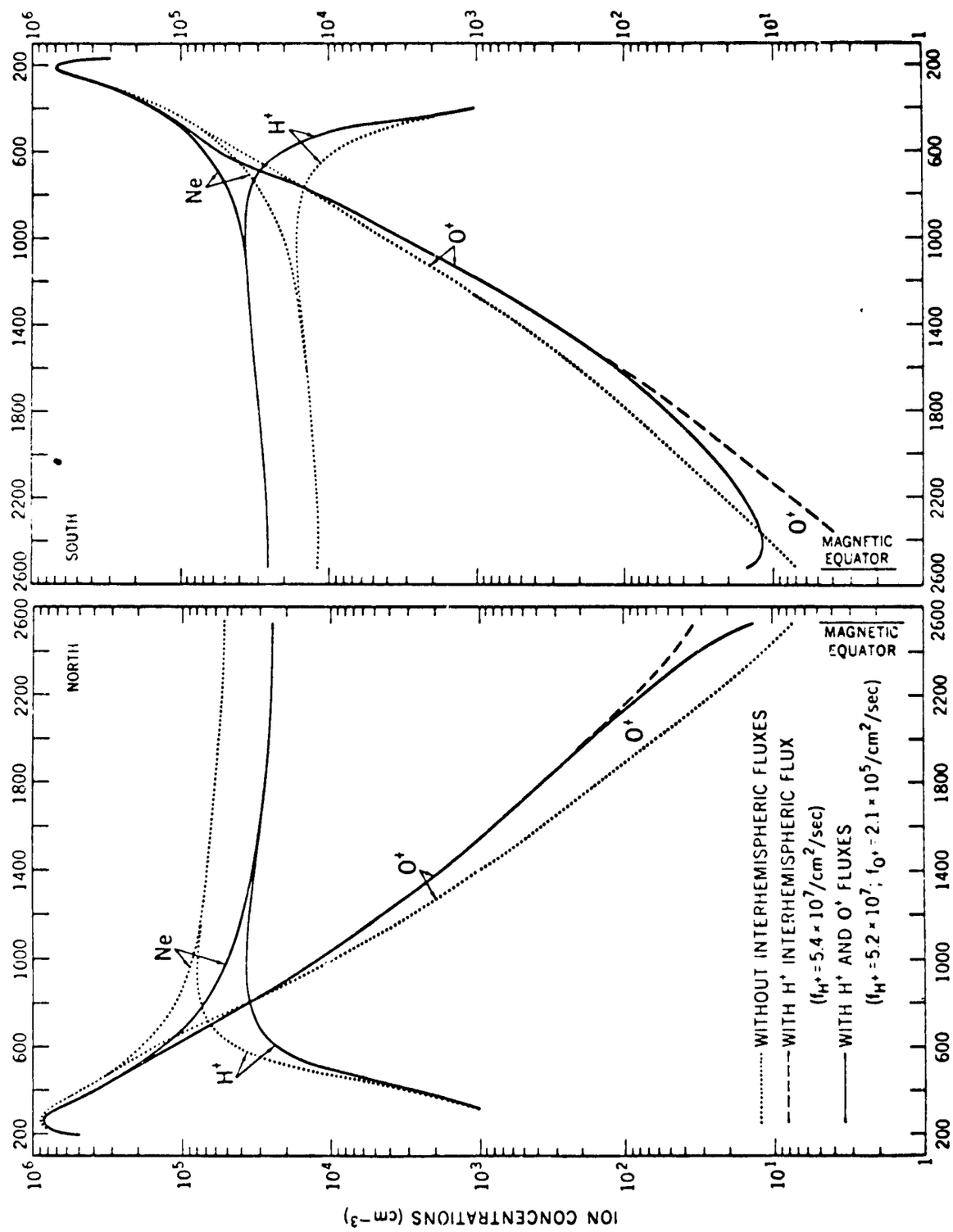

Figure 3. Calculated composition profiles with and without interhemispheric fluxes.

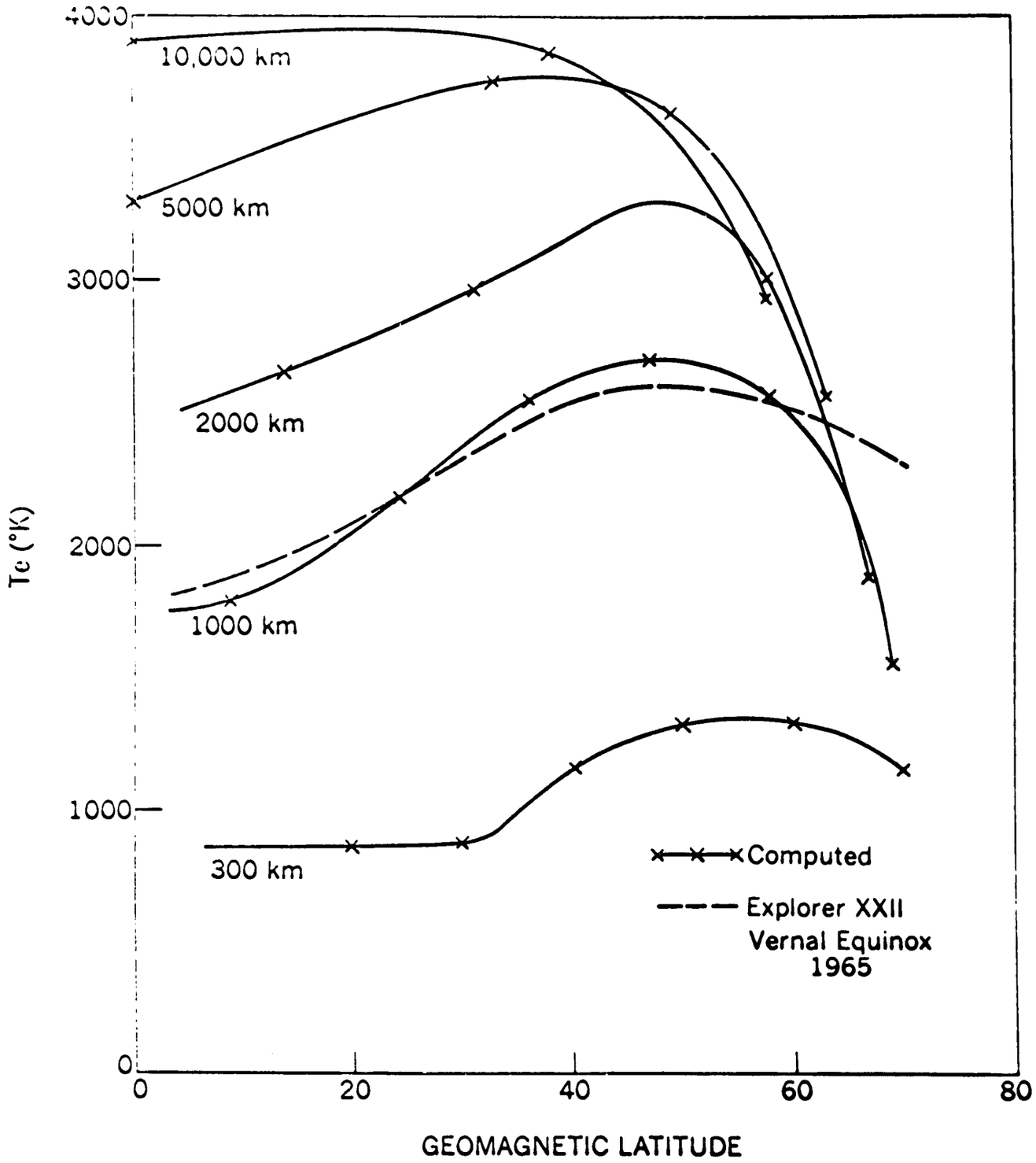

Figure 4. Computed latitudinal electron temperature distribution for various altitudes (solid curves). For comparison the electron temperature at 1000 km from Explorer XXII, vernal equinox 1965, (Brace et al., 1967) is shown in the dashed curve.

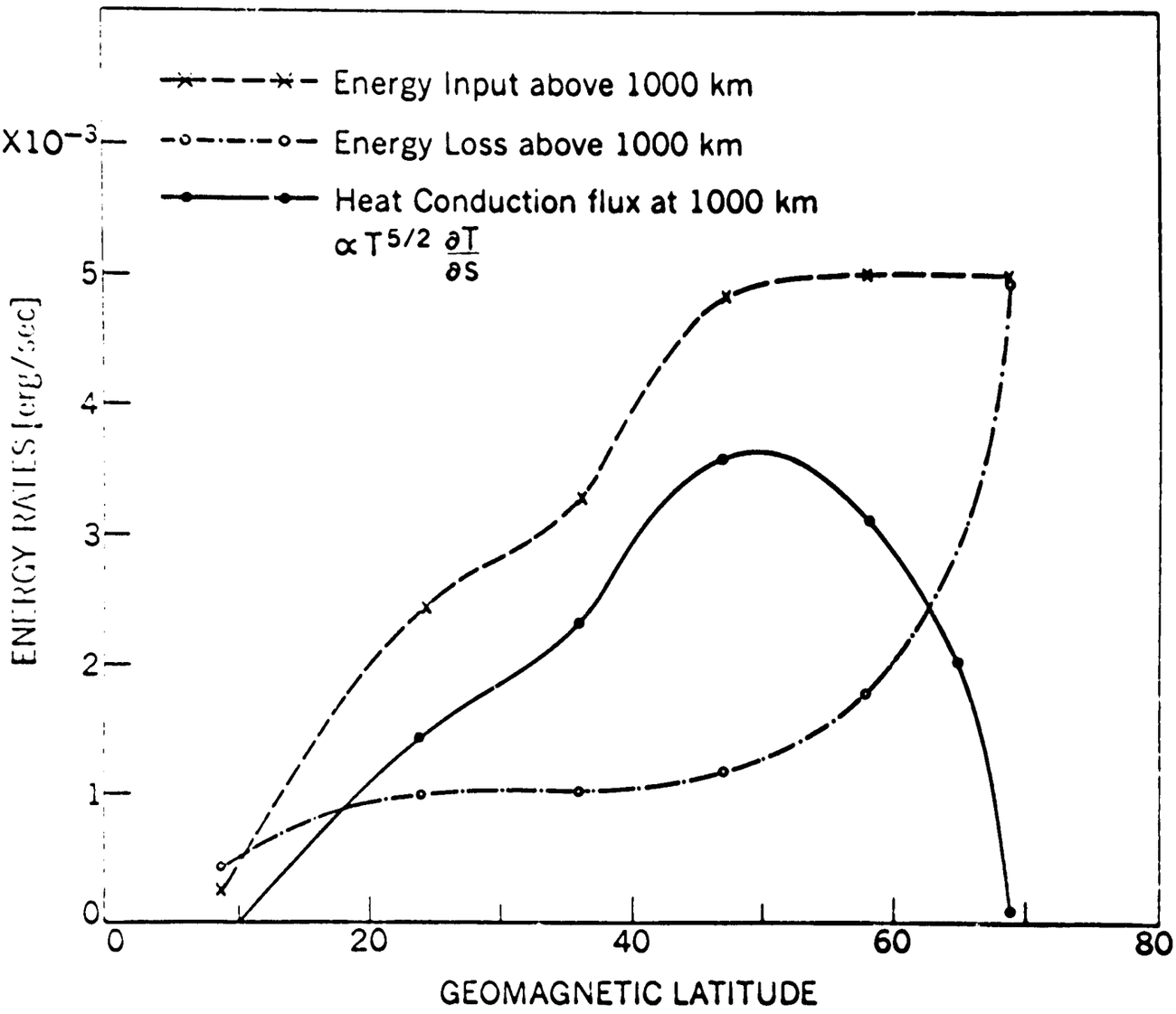

Figure 5. Energy rates integrated over the field tube volumes above 1000 km (with base area of 1 cm^2) as a function of the latitude at the base of the field line.

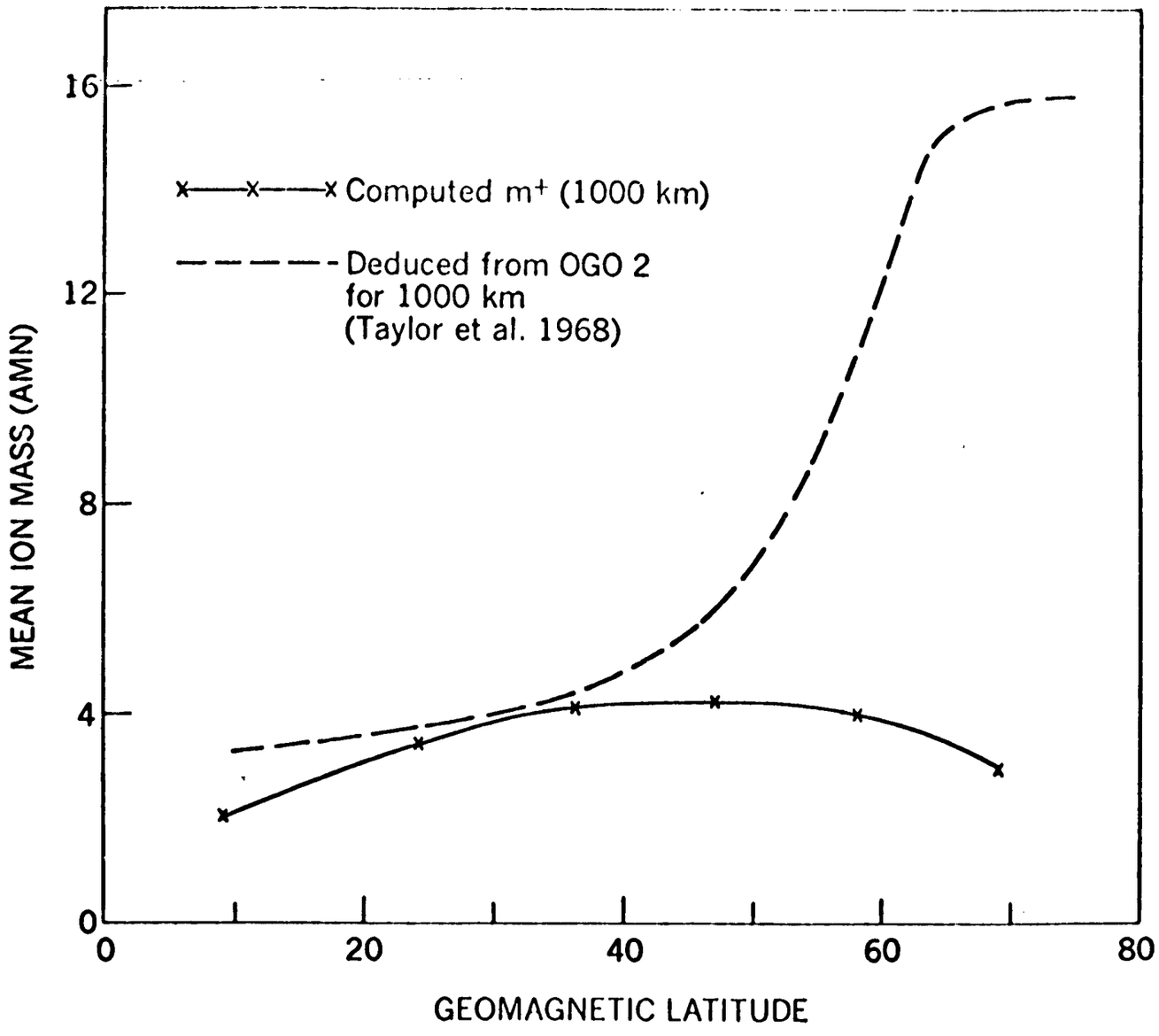

Figure 6. Computed mean ion mass at 1000 km. For comparison the mean ion mass deduced for 1000 km from OGO 2 results (Taylor et al., 1968) is shown for dusk, October 1965.

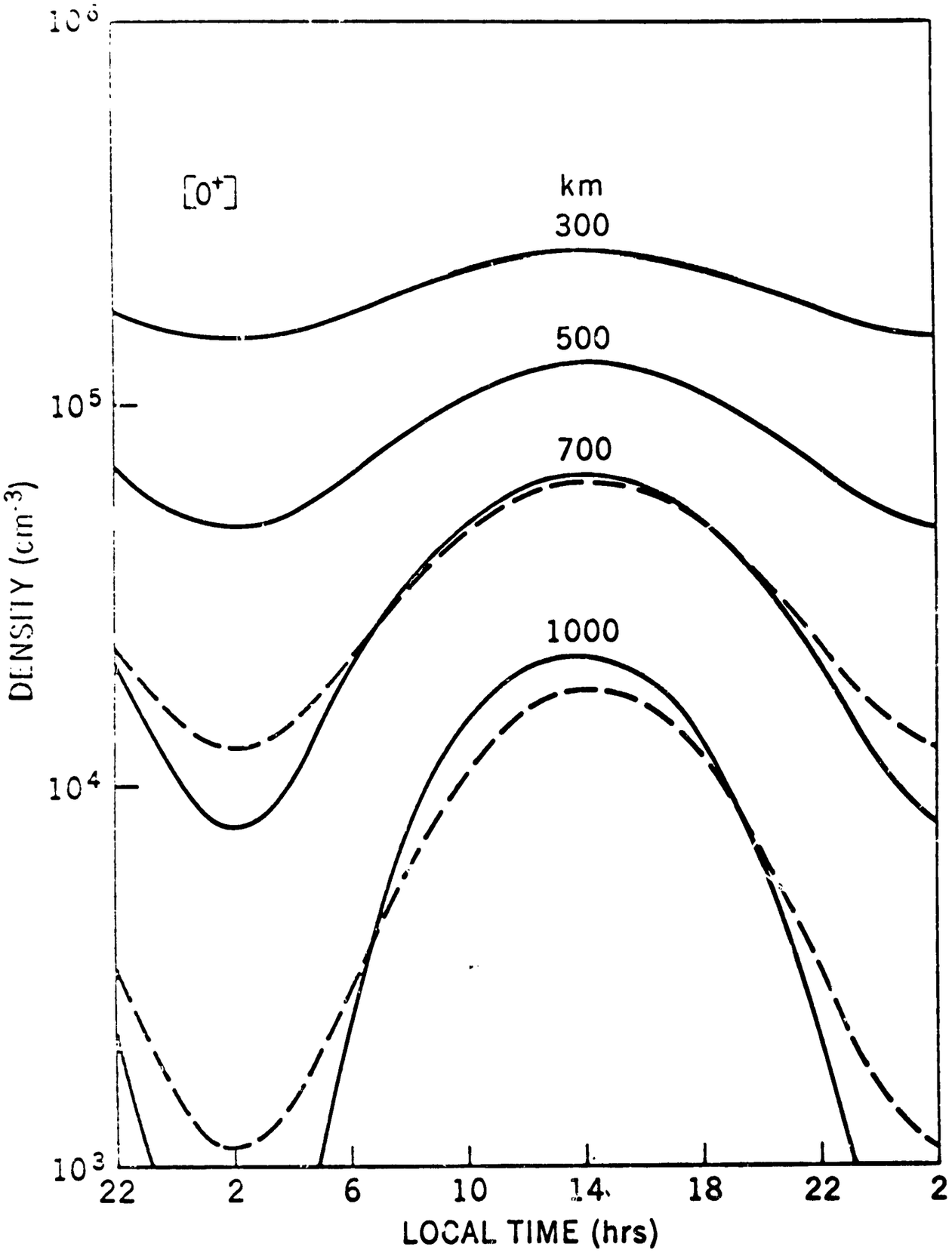

Figure 7. Computed temporal distribution of O^+ at various altitudes. The solid curves represent the time-dependent solution and the dashed curves the quasi-stationary solution ($\partial/\partial t = 0$).

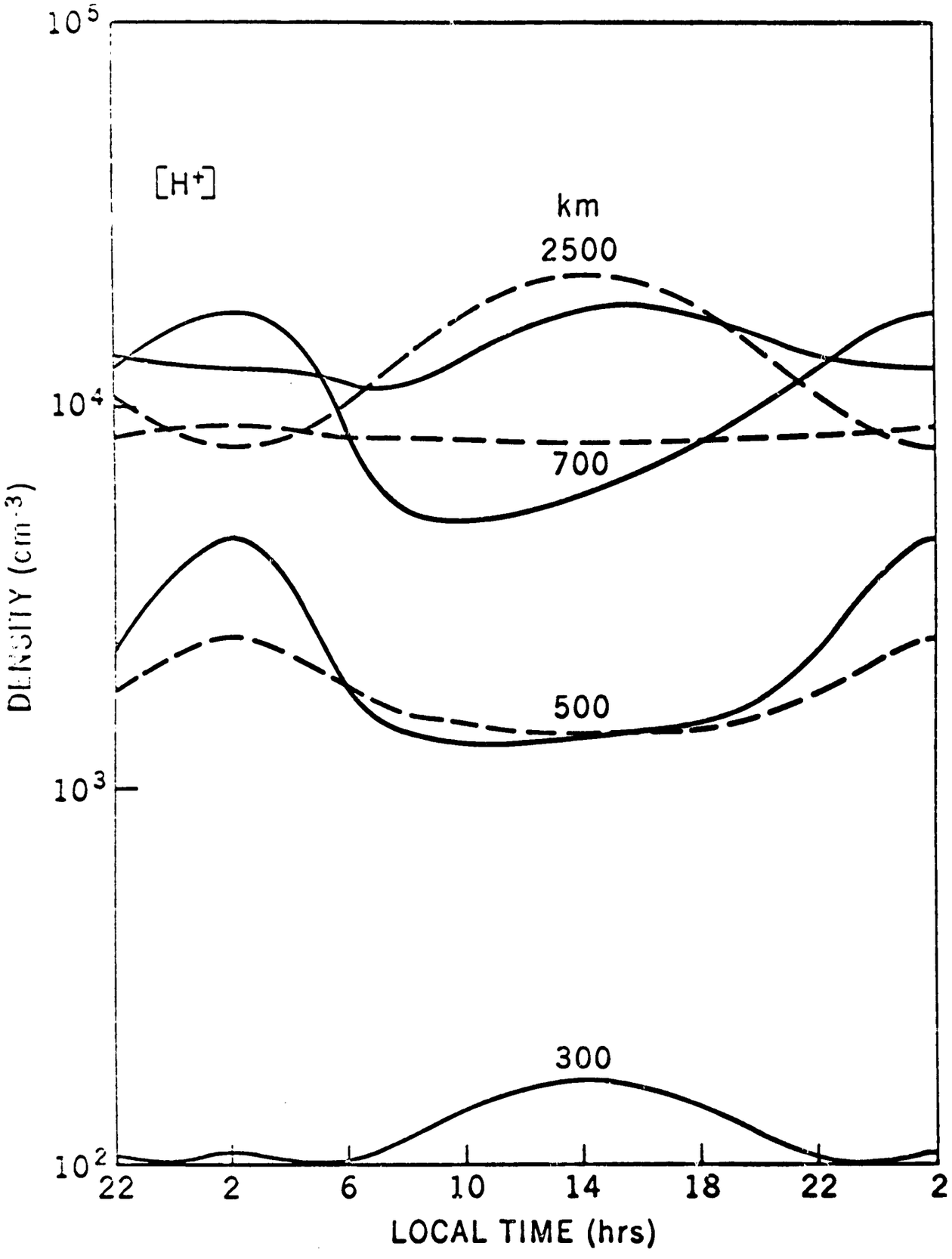

Figure 8. Computed temporal distribution of H^+ at various altitudes. The solid curves represent the time-dependent solution and the dashed curves the quasi-stationary solution ($\partial / \partial t = 0$).

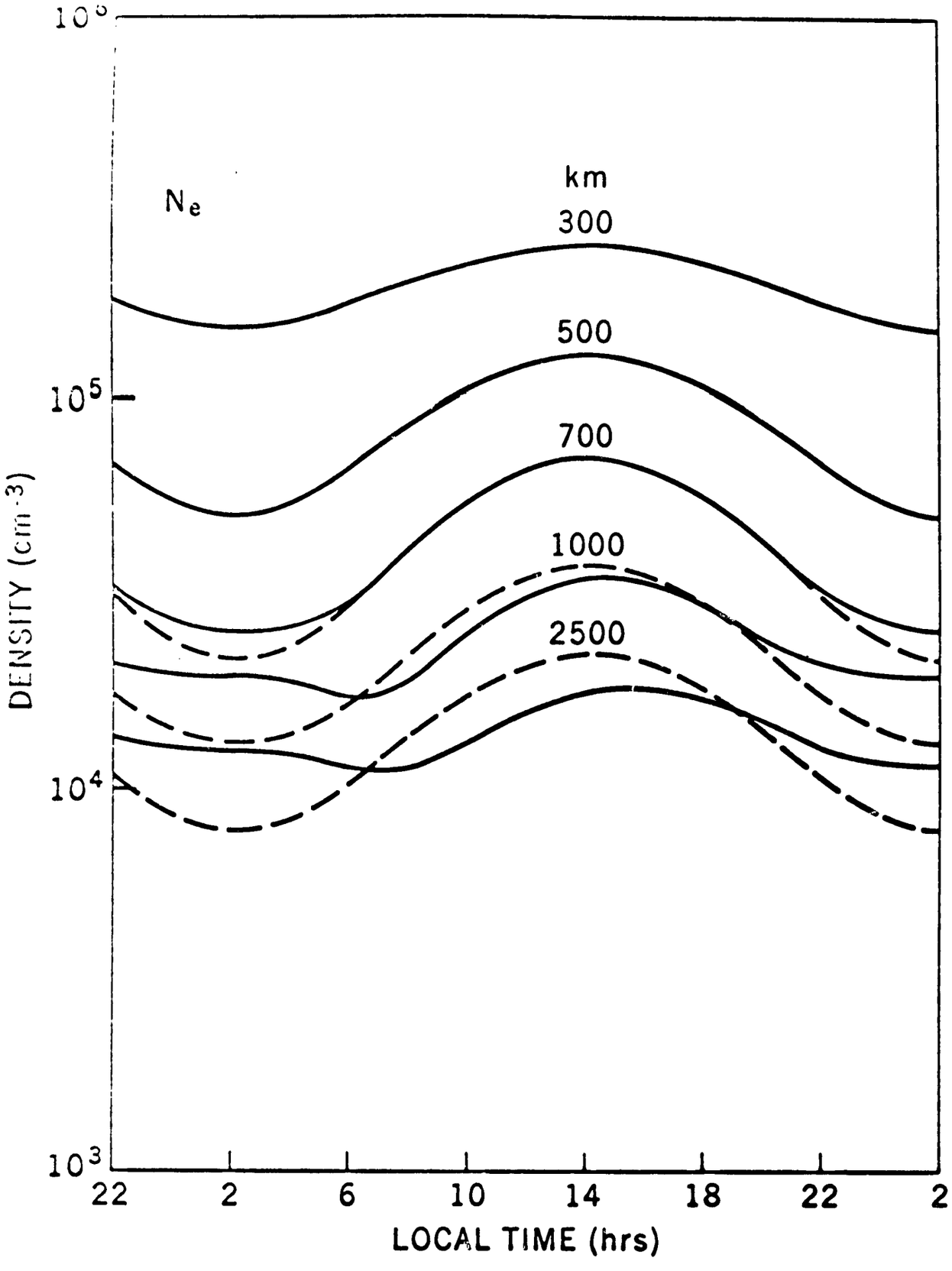

Figure 9. Computed temporal electron density distribution at various altitudes. The solid curves represent the time-dependent solution and the dashed curves the quasi-stationary solution ($\partial / \partial t = 0$).

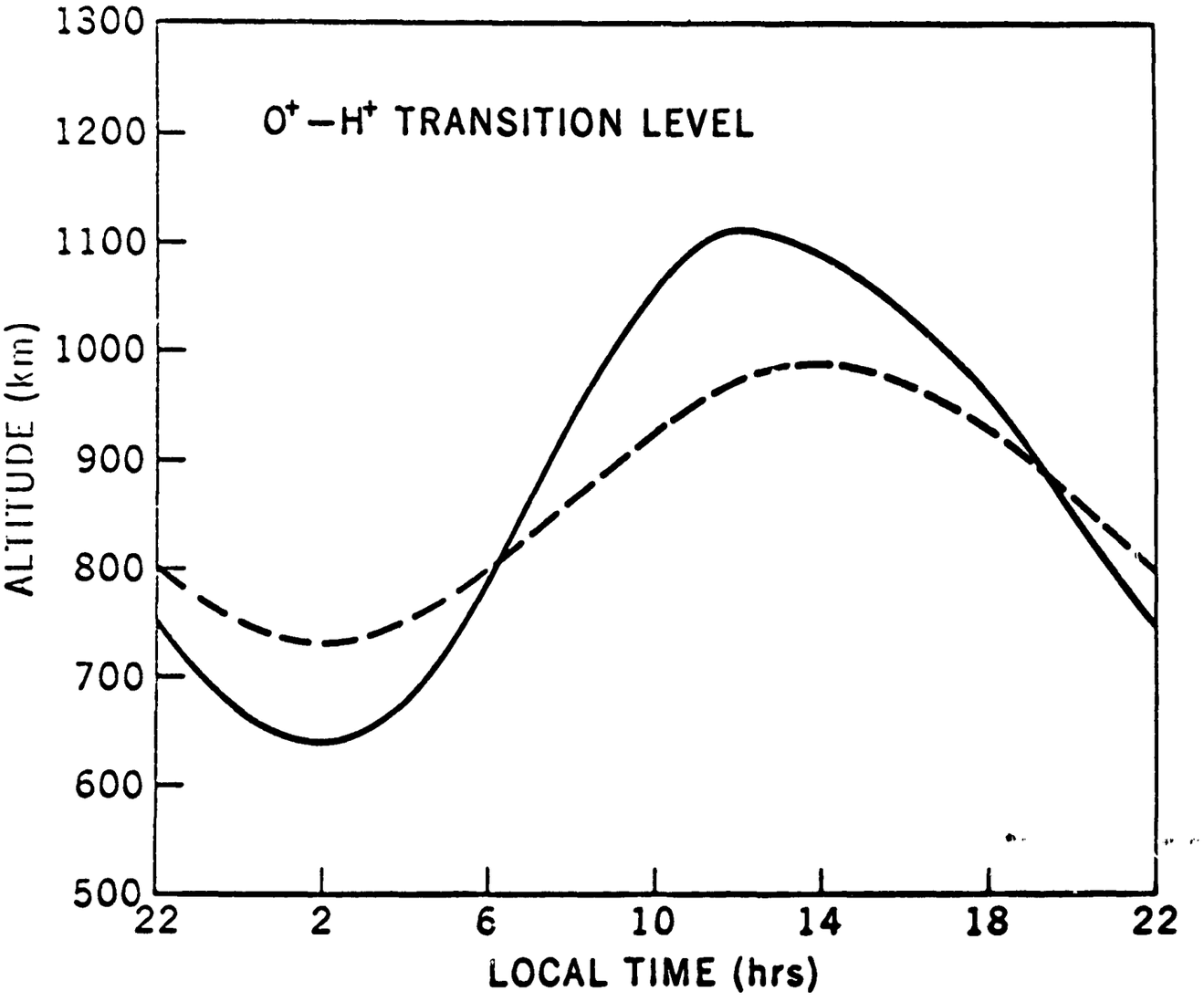

Figure 10. Computed temporal variation of the O^+-H^+ transition level. The solid curve represents the time-dependent case and the dashed curve the quasi-stationary case ($\partial / \partial t = 0$).